Quantifying the Radiative Impact of Clouds on Tropopause Layer Cooling in Tropical Cyclones

LOUIS RIVOIRE

Department of Atmospheric Science, Colorado State University, Fort Collins, Colorado

THOMAS BIRNER

Meteorological Institute, Ludwig-Maximilians-Universität München, Munich, Germany

JOHN A. KNAFF

NOAA/Center for Satellite Applications and Research, Fort Collins, Colorado

NATALIE TOURVILLE

Cooperative Institute for Research in the Atmosphere, Colorado State University, Fort Collins, Colorado

ABSTRACT

A ubiquitous cold signal near the tropopause, here called "tropopause layer cooling" (TLC), has been documented in deep convective regions such as tropical cyclones (TCs). Temperature retrievals from the Constellation Observing System for Meteorology, Ionosphere, and Climate (COSMIC) reveal cooling of order 0.1–$1 \, \mathrm{K \, day^{-1}}$ on spatial scales of order $1000 \, \mathrm{km}$ above TCs. Data from the Cloud Profiling Radar (onboard *CloudSat*) and from the Cloud–Aerosol Lidar with Orthogonal Polarization [onboard the *Cloud–Aerosol Lidar and Infrared Pathfinder Satellite Observations* (*CALIPSO*)] are used to analyze cloud distributions associated with TCs. Evidence is found that convective clouds within TCs reach the upper part of the tropical tropopause layer (TTL) more frequently than do convective clouds outside TCs, raising the possibility that convective clouds within TCs and associated cirrus clouds modulate TLC. The contribution of clouds to radiative heating rates is then quantified using the *CloudSat* and *CALIPSO* datasets: in the lower TTL (below the tropopause), clouds produce longwave cooling of order 0.1–$1 \, \mathrm{K \, day^{-1}}$ inside the TC main convective region, and longwave warming of order 0.01–$0.1 \, \mathrm{K \, day^{-1}}$ outside; in the upper TTL (near and above the tropopause), clouds produce longwave cooling of the same order as TLC inside the TC main convective region, and one order of magnitude smaller outside. Considering that clouds also produce shortwave warming, cloud radiative effects are suggested to explain only modest amounts of TLC while other processes must provide the remaining cooling.

1. Introduction

The region between the tropical troposphere and stratosphere is best described as a transition layer, usually referred to as the tropical tropopause layer (TTL). The TTL is defined by Fueglistaler et al. (2009) between ∼14 and 18.5 km above sea level (∼150 to 70 hPa), with the climatological cold-point tropical tropopause located near 17 km (Seidel et al. 2001). Due to its nature, the TTL is subject to influences from both tropospheric and stratospheric processes. From above, planetary-scale circulations in the stratosphere influence the TTL on intraseasonal to interannual time scales (Angell and Korshover 1964; Reid and Gage 1985). From below, mesoscale deep convective systems produce large temperature anomalies in the TTL (Jordan 1960; Johnson and Kriete 1982; Randel et al. 2003; Holloway and Neelin

---

ⓐ Denotes content that is immediately available upon publication as open access.

Corresponding author: L. Rivoire, lrivoire@colostate.edu

2007; Paulik and Birner 2012; Kim et al. 2018), and alter its chemical composition (e.g., Danielsen 1993; Jensen et al. 2007) and its radiative flux balance (Thuburn and Craig 2002; Gettelman et al. 2002; Kuang and Bretherton 2004) by lofting air from the boundary layer into the TTL on time scales of a few hours. As a result of the above influences, the energy budget in the TTL is complex and each contribution needs to be quantified.

In this work, we seek to quantify the contribution of cloud radiative processes to anomalous temperature signals found in the TTL above tropical cyclones (TCs). Specifically, Arakawa (1951), Koteswaram (1967), Biondi et al. (2013), and Rivoire et al. (2016) have identified cooling within a layer a few kilometers deep surrounding the tropopause above TCs. We will refer to this ubiquitous signal as "tropopause layer cooling" (TLC hereafter). The primary motivation for this study is the limited understanding of plausible feedbacks between TLC and the structure and dynamics of underlying TCs. Anomalously low temperatures near the tropopause decrease the static stability (i.e., the resistance to vertical displacements) in the TTL, implying stronger updrafts in the upper troposphere and higher cloud tops. Potential impacts include vertical advection of angular momentum by convective bursts and a corresponding upper-tropospheric cyclonic circulation and warm core, which Ohno and Satoh (2015) described inside the eyewall, and which translated to abrupt TC intensity changes in numerical simulations (Zhang and Chen 2012; Chen and Zhang 2013). The destabilization of the upper troposphere may also modulate the stratification and vertical extent of the TC outflow layer, thereby impacting TC motion (Flatau and Stevens 1993), structure (Holland and Merrill 1984), and intensity (Doyle et al. 2017). An improved characterization of upper-level processes in TCs is needed in order to establish better understanding of these feedbacks.

Existing literature gives several motives to focusing on cloud radiative effects above TCs. While the occurrence frequency of convective clouds decays with height nearly exponentially above 12 to 14 km in the tropics (Gettelman et al. 2002), convective regions greatly impact the radiative flux balance of the TTL (Thuburn and Craig 2002; Yang et al. 2010). Additionally, deep convection within TCs has been described by proxy to reach the uppermost troposphere and penetrate the stratosphere more frequently than isolated convection (Romps and Kuang 2009), particularly in the western North Pacific Ocean. It is therefore a reasonable expectation that sustained deep convection in TCs—among all marine deep convective systems—may have a disproportionately large impact on the chemical composition
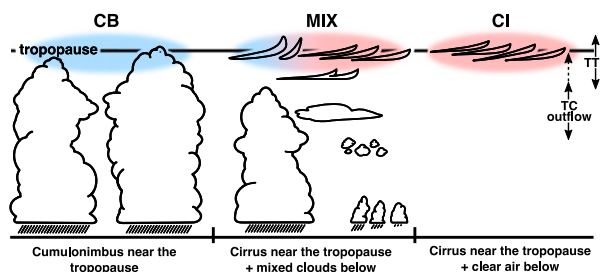

FIG. 1. Schematic highlighting three typical cloud scenarios and associated qualitative longwave radiative flux divergence expected near the tropopause, with blue for divergence (cooling) and red for convergence (warming). Cumulonimbus are represented as tall, billowy shapes. Cumulus are represented as shallower billowy shapes. Cirrus are represented as upper-level, horizontally elongated shapes. Other shapes represent midlevel clouds (altostratus, nimbostratus, stratocumulus, stratus, and altocumulus).

of the TTL (Ray and Rosenlof 2007) and therefore on the radiative flux balance of the TTL. Deep convective clouds exhibit longwave cooling near their top and shortwave heating below, which could also impact the radiative flux balance of the TTL. Closely associated with deep convection and TCs are cirrus clouds, which can detrain from the top of cumulonimbus as extensive anvils or form in situ via turbulent mixing (Jensen et al. 1996). The longwave radiative impacts of cirrus occurring near the tropopause depend on the underlying atmosphere (Ackerman et al. 1988; Hartmann et al. 2001): when the troposphere is clear, cirrus are generally expected to lead to warming by absorbing more upwelling longwave radiation from the surface than they emit near their top. When the troposphere is populated with stratiform, stratocumuliform, low, or thin clouds, the same is generally true and cirrus warm the tropopause. When the troposphere is populated with deep convective clouds, cirrus can cool the tropopause by emitting more longwave radiation near their top than they absorb from the cold cloud tops below (see Hartmann et al. 2001). These effects are illustrated in Fig. 1.

At present, quantitative knowledge of cloud vertical distribution in TCs remains limited, posing strong limitations for radiative computations (Corti et al. 2005). Cloud boundaries are subject to large errors; for instance, cloud top heights estimated from infrared brightness temperature retrievals are subject to errors ~1 km due to varying cloud optical properties and to the presence of cirrus aloft that are difficult to distinguish from convective clouds using passive sensors alone (see Hawkins et al. 2008). In our study, these caveats are alleviated by using the cloud classification product from Sassen et al. (2008) and radiative heating rates from

Henderson et al. (2013), both of which are derived from the combination of *CloudSat*'s radar and *CALIPSO*'s[1] lidar retrievals, conferring their detection capability for optically thick as well as thin clouds (Sassen et al. 2009). Data available near active TCs are compiled in the *CloudSat* TC overpass dataset (Tourville et al. 2015). For the portion of the analysis relevant to quantifying TLC, we use high-vertical-resolution, high-accuracy temperature retrievals from the Constellation Observing System for Meteorology, Ionosphere, and Climate (COSMIC) as in Rivoire et al. (2016).

We focus on TCs in the tropical western North Pacific Ocean. We first quantify the total temperature tendencies associated with TLC using COSMIC data. We then characterize the vertical profiles of longwave radiative heating inside TCs associated with the cloud scenarios of interest (see Fig. 1). Last, we quantify the overall longwave radiative effect of clouds in TCs. A description of our compositing technique is provided in section 2 along with further details about the datasets we use. The results of our analysis are presented in section 3 and discussed in section 4.

2. Data and methods

Data come from two primary sources for this study: the *CloudSat* TC overpass dataset, and the COSMIC Data and Archiving Center.

a. Cloud classification product

The cloud classification product (2B-CLDCLASS-lidar version R05) is derived from the combination of collocated spaceborne radar and lidar data, owing to *CloudSat* and *CALIPSO* flying the same orbit for extended periods of time with a separation time of only ~8.5 s. Data are given at the 240-m maximum vertical resolution of *CloudSat*'s Cloud Profiling Radar (CPR) and with a ~1.5-km horizontal resolution: to each radar volume corresponds one of eight cloud types determined using a fuzzy-logic-based algorithm. Generally speaking, cloud type (stratus, stratocumulus, altocumulus, cumulus, nimbostratus, altostratus, cumulonimbus, or cirrus) is determined using cloud features (reflectivity, water phase, temperature, height, vertical and horizontal extent, homogeneity, and precipitation) derived from the products listed in section 2b.[2]

Few data are available to evaluate the performance of the 2B-CLDCLASS-lidar product in terms of high, thin clouds detectable by lidar only. However, Sassen and Wang (2008) found their radar-only *CloudSat* cloud classification product (2B-CLDCLASS) to be in good agreement with cloud classification products created prior [from ground reports (see Hahn and Warren 1999) and from the International Satellite Cloud Climatology Project (ISCCP; see Rossow and Schiffer 1999)]. The radar–lidar cloud classification product is therefore expected to be in good agreement with other classification products, while improving the characterization of high, thin clouds.

The cloud scenarios described in Fig. 1 are named CB (cumulonimbus reaching near the tropopause), MIX (cirrus near the tropopause and mixed clouds below), and CI (cirrus near the tropopause and clear air below). We use cloud boundary heights from the 2B-CLDCLASS-lidar product and proceed as follows:

- The cloud top height of the uppermost cloud layer (cumulonimbus for CB, cirrus for CI and MIX) must be located within 1 km of the average height of the cold-point tropopause (i.e., it must be located between 16 and 18 km above sea level). All cases with clouds above 18 km are consequently excluded.
- For CB, there can only be cumulonimbus clouds in the column, and at least one cumulonimbus layer must be at least 10 km deep (this criterion is almost always met as cumulonimbus are classified as such in part according to their large vertical extent).
- For CI, there can only be cirrus clouds in the column, and cirrus must occur in one layer no thicker than 5 km. Cases with thickness greater than 5 km are included in the MIX scenario.
- MIX includes all combinations of cloud types in any number of layers, as long as the uppermost cloud layer is classified as cirrus.

From a total of 264 645 retrievals located within 1000 km of active, intensifying TCs, 74 067 (38%) contain no hydrometeors. Among the remaining 190 578 retrievals that do contain hydrometeors, our method classifies 6% as CB, 30% as MIX, and 2% as CI. Approximately 9% exhibit a cloud layer (of any cloud type) with its top between 16 and 18 km but that does not meet the criteria for either cloud scenario. Less than 1% of retrievals meet either cloud scenario criterion but are rejected because their uppermost cloud layer (cirrus or cumulonimbus that is) is located above 18 km. Consequently, choosing a different near-tropopause layer than 16–18 km has little effect on our results. The thickness criterion for the CI scenario (5 km) corresponds to the median geometric thickness of all isolated cirrus layers

---

[1] Cloud–Aerosol Lidar and Infrared Pathfinder Satellite Observations.

[2] Details of the method and algorithm are available in Sassen and Wang (2012) and in the algorithm release documentation (http://www.cloudsat.cira.colostate.edu).

with their top between 16 and 18 km. Using this criterion allows us to produce a large sample size and to eliminate the thickest cirrus layers for which the longwave radiative effects tend to maximize below the tropopause (i.e., cases that are not directly relevant to the impact of cloud radiative effects on the tropopause). Choosing a smaller thickness criterion (e.g., 4 km) does not impact the qualitative results and only reduces the size of the sample. The CI scenario could also be defined using a cloud optical thickness threshold for cirrus layers, instead of using a geometric thickness threshold. Doing so would confer the advantage of including in CI some cirrus layers that are optically thin but have varying geometric thickness. For the sake of compositing, however, given the general correlation between geometric and optical thickness, this alternate method is not expected to impact the results. Additionally, the absence of comparable datasets for cloud optical thickness makes assessing uncertainties difficult.

b. Radiative heating rates

The "radar–lidar fluxes and heating rates" product (2B-FLXHR-lidar version R04) consists of vertically resolved radiative fluxes and heating rates derived from the combined *CloudSat* and *CALIPSO* data. Radiative fluxes and heating rates are given with the same resolution as the 2B-CLDCLASS-lidar product. Radiative fluxes are calculated using the Bugsrad radiative scheme (Fu and Liou 1992; Stephens et al. 2001) that models molecular scattering, gaseous absorption, and absorption and scattering by liquid water and ice water. Inputs to the radiative transfer model are the following:

- Cloud locations from the "radar–lidar cloud geometric profile" product (2B-GEOPROF-lidar; Mace et al. 2009), which is derived from radar reflectivity and lidar backscatter data.
- Cloud properties (ice and liquid water content, equivalent mass sphere effective radius of hydrometeors) determined using the "cloud water content (radar only)" product (2B-CWC-RO; Austin et al. 2009) for clouds detectable by the CPR, the MODIS[3]-based "optical depth" product (2B-TAU), and collocated CALIPSO products (Trepte et al. 2010) for clouds detectable by lidar only, and the "precipitation column" product (2C-PRECIP-COLUMN; Haynes et al. 2009).
- Temperature, humidity, and ozone concentration profiles from the European Centre for Medium-Range

Weather Forecasts (ECMWF) analyses (ECMWF-AUX product).
- Surface albedo and emissivity data from the International Geosphere–Biosphere Programme global land surface classification (Townshend 1992).

We use the longwave radiative fluxes for this study and leave the shortwave radiative fluxes aside as they are known to suffer larger uncertainties (Henderson et al. 2013) and are not directly relevant to explaining the presence of cooling in the atmosphere.

The 2B-FLXHR-lidar product is an improvement of the 2B-FLXHR product (L'Ecuyer et al. 2008), which did not include lidar data. Estimating uncertainties for the vertically resolved radiative flux products is difficult due to the lack of a similar dataset. However, comparisons of top-of-atmosphere fluxes between the 2B-FLXHR-lidar and 2B-FLXHR products and the CERES[4] product show close correlation and show an improvement from 2B-FLXHR algorithm to the 2B-FLXHR-lidar algorithm (Henderson et al. 2013) due to the improved characterization of high, thin clouds undetectable with *CloudSat*'s CPR alone (below ~30 dBZ). Global mean uncertainties from the inputs to the algorithm listed above were estimated by introducing perturbations to each input (Henderson et al. 2013): assumptions made for the effective radius of hydrometeors introduce errors of order 0.1–1 W m^{-2} to outgoing longwave radiation (OLR), which is comparable to uncertainties introduced by resolution related errors on cloud boundary (top and base) heights. For reference, mean OLR is ~250 W m^{-2} above the western North Pacific Ocean, with ~5 W m^{-2} contributed by high, thin clouds. Uncertainties in OLR introduced by errors in the tropospheric temperature and humidity profiles from the ECMWF-AUX products are estimated to be of order 1 W m^{-2}. Although uncertainties associated with errors in ozone concentration profiles have not yet been estimated for the *CloudSat* products, results in Gettelman et al. (2004) and Birner and Charlesworth (2017) show that ozone is not a primary contributor to heating rates in the TTL. Additionally, ozone concentrations can be especially low in the TTL over the western North Pacific when deep convection transports air from the ozone-poor marine boundary layer (Gettelman et al. 2004).

The contribution of clouds (hydrometeors) to the radiative heating rates is referred to as the "cloudy-sky" term and is calculated as the difference between the "all-sky" term (the overall heating rate) and the "clear-sky"

---

[3] Moderate Resolution Imaging Spectroradiometer.

[4] Clouds and the Earth's Radiant Energy System.

term (the contribution from gases like water vapor). Since the clear-sky radiative heating rates are not directly provided in the *CloudSat* dataset, we calculate them from the clear-sky radiative flux profiles using

$$\mathrm{HR} = \frac{g}{c_p}\frac{dF}{dp},$$

where HR is the heating rate ($\mathrm{K\,s}^{-1}$), g is the gravitational acceleration ($\sim 9.81\,\mathrm{m\,s}^{-2}$), c_p is the specific heat capacity of dry air at constant pressure ($\sim 1005\,\mathrm{J\,K}^{-1}\,\mathrm{kg}^{-1}$), p is the atmospheric pressure (Pa; from the ECMWF-AUX product), and F is the radiative flux ($\mathrm{W\,m}^{-2}$; from the 2B-FLXHR-lidar product) defined as the difference between the upwelling and downwelling radiative fluxes at each vertical level. The pressure derivative of the radiative flux is estimated numerically using finite differences.

c. COSMIC temperature retrievals

The COSMIC Data Analysis and Archive Center uses the radio occultation technique to provide temperature retrievals globally, for all weather conditions, and with high vertical resolution ($\sim 200\,\mathrm{m}$). Radio waves emitted by the global positioning system (GPS) satellites are detected by COSMIC satellites in low Earth orbit. When the line of sight between GPS and COSMIC satellites passes through the atmosphere, radio waves are refracted depending on the state of the atmosphere—primarily its temperature, pressure, and water vapor content (see Kursinski et al. 1997). At altitudes where the temperature is below 250 K (generally above $\sim 10\,\mathrm{km}$ in the tropics), the contribution of water vapor to refraction is considered negligible (Kursinski et al. 1996) and the "dry" temperature is retrieved by approximating the pressure via downward integration of the hydrostatic equilibrium equation from the top of the atmosphere. The refraction of radio waves also includes a small contribution from ice water. However, given the small ice water content in high-altitude clouds retrieved by *CloudSat* and *CALIPSO* (10^{-3} to $10^{-2}\,\mathrm{g\,m}^{-3}$), the ice water contribution is expected to be 5 to 6 orders of magnitude smaller than the contribution of temperature and pressure, and is therefore neglected.

In the upper troposphere and lower stratosphere, the precision of individual COSMIC temperature retrievals was estimated near 0.05 K by comparing collocated retrievals (Anthes et al. 2008). The accuracy of COSMIC refractivity retrievals was estimated as a departure from other independent datasets near 0.1%–0.5% in the upper troposphere and lower stratosphere, yielding temperature errors of order 0.1–1 K assuming a dry atmosphere (Kuo et al. 2004; Anthes et al. 2008). The

GPS radio occultation technique does not provide vertical atmospheric soundings; rather, temperature retrievals are inclined and typically span $\sim 100\,\mathrm{km}$ horizontally from their top ($\sim 60\,\mathrm{km}$ above sea level) to their bottom. Since the region of interest in this study (~ 12–$20\,\mathrm{km}$) is relatively shallow, horizontal drift is neglected.

Note that temperature retrievals are available that account for the contribution of water vapor to refractivity. These "wet" retrievals are derived using temperature data from the ECMWF analyses, which means that the retrievals are subject to errors in the analyses. Near regions of steep gradients such as TCs, these errors can be large and yield large temperature biases (see Davis and Birner 2016). The so-called wet retrievals are therefore not included in our study.

d. Compositing philosophy and method

In this study, we quantify processes that are tied to the structure of TCs—structure that varies significantly from storm to storm. To eliminate this variability and draw conclusions that are broadly relevant to the robust features found in TCs, observations are composited from a large number of events. Compositing data also allows us to alleviate the sparse nature of the COSMIC and A-Train datasets. No individual storm is sampled by either platform with coverage sufficient to provide meaningful information regarding cloud processes and tropopause heights. Since the features we observe are prone to producing heavily skewed distributions (e.g., cloud top heights; see Fig. 2), compositing data based on the mean would yield skewed results. Instead, statistics are provided as the median, a more robust measure of central tendency here. Whenever appropriate, we supplement the median with a robust measure of statistical spread chosen as the interquartile range (the 25th–75th percentiles).

The compositing time period is 1 January 2007–17 April 2011. Both COSMIC and A-Train radar–lidar products are available for this period. Radar–lidar products are scarcely available after 17 April 2011 due to changes in *CloudSat*'s orbit initially caused by a battery anomaly. During the compositing time period, since satellites on the A-Train flew a sun-synchronous orbit with equator local crossing times of 0130 and 1330 (Stephens et al. 2002), the A-Train products are biased toward the local time of observation. However, we do not expect this to be problematic for the interpretation of our results since the diurnal cycle of convection is a relatively small source of variability in the distribution of convection in TCs when compared to sources of variability such as TC size, intensity, and convective asymmetries (Knaff et al. 2015, 2019). Additionally, the
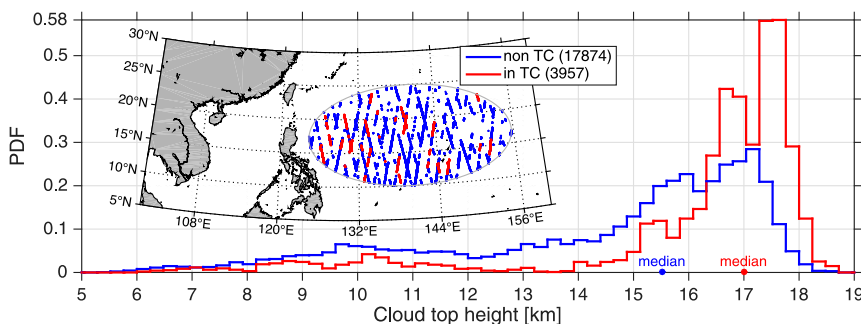
FIG. 2. Histograms of deep convective cloud top heights in the region of the tropical west Pacific indicated in the inset map for 1 Jan 2007–17 Apr 2011. Retrievals located within 200 km of active TCs are in red. Retrievals not associated with active TCs are in blue. The number of samples is shown in the legend.

local equator crossing times for the A-Train reasonably sample the convective extrema, both in terms of area covered and heights reached (Liu and Zipser 2008).

The compositing region is the tropical portion of the western North Pacific Ocean (0°–25°N, 100°E–180°). As mentioned earlier, the western North Pacific most frequently generates TCs with deep convective clouds reaching the TTL and penetrating the stratosphere (Romps and Kuang 2009). The western North Pacific also accounts for roughly a third of TCs globally (Neumann 1993) and is a good candidate for collecting a large data sample and produce robust composites. Indeed, a total of 102 TCs formed there virtually year-round during the 2007–11 time period, with highest activity in August–October (and lowest activity in January–March). In order to limit the influence of extratropical processes associated with large gradients of sea surface temperatures (Reynolds and Smith 1995), ambiguous tropopause heights and large gradients of tropopause temperatures (Seidel et al. 2001), and large magnitudes of deep-layer wind shear, data are excluded when located poleward of 25°N or when associated with TCs which center is located poleward of 25°N. Data are also excluded when located over land.

Data are collected in the vicinity of intensifying TCs based on best track locations and intensities from the Automated Tropical Cyclone Forecasting system (ATCF; Sampson and Schrader 2000). Best track uncertainty estimates are typically 15–40 nautical miles (28–74 km) in terms of location and 8–12 kt (4–6 m s^{-1}) in terms of intensity (Knaff et al. 2010; Torn and Snyder 2012). These uncertainties are small for the purpose of compositing at large distances from the TC center. Closer to the TC center, these uncertainties produce smoothing comparable to that introduced by varying TC size and by the choice of horizontal resolution of the composites. The radiative

heating rates and cloud classification products are directly composited along the spatial dimensions (radius, altitude). Calculating temperature tendencies from COSMIC temperature retrievals requires the use of a time dimension; here time relative to the time of first maximum intensity calculated from the ATCF best tracks for each TC. This time dimension preserves the chronology of the TC life stages about maximum intensity, that is, intensification and weakening. We focus on the intensification period for the purpose of this study, primarily because the coldest clouds (highest, by proxy) occur during intensification and warm rapidly after maximum intensity (e.g., Rivoire et al. 2016). Since TCs reach their maximum intensity near 18°–20°N in the western North Pacific, removing the weakening period from the composites also reduces biases that occur where data are collected only on the equatorward side of the TC center when best tracks near the northern edge of the compositing region (25°N).

3. Results

a. Cloud distributions

The findings of Romps and Kuang (2009) about overshooting convection in TCs relied on reanalysis datasets and proxies available at the time, both of which suffer known biases and resolution limitations (which the authors discuss). Prior literature on the topic (e.g., Alcala and Dessler 2002; Cairo et al. 2008) also suffers limitations in terms of hydrometeor detection above the oceans. It seems appropriate to provide updated statistics relevant to deep convective clouds, especially comparing cloud top heights for deep convective clouds that are associated with TCs versus those that are not. Figure 2 provides such a comparison using cloud

top heights calculated using the 2B-CLDCLASS-lidar product. Cloud top heights are collected within a subregion of the tropical western North Pacific climatologically encompassing most tracks and tropical cyclogenesis events. The difference between the two distributions clearly indicates that deep convection reaches greater altitudes when associated with TCs (within 200 km of TCs). The median deep convective cloud top height outside TCs is 1.5 km lower than inside TCs. Half of all clouds inside TCs reach above 17 km, which nearly corresponds to the median height of the tropopause (16.9 km; see section 3b). One cannot say conclusively that these clouds penetrated the local tropopause; doing so would require collocated cloud top and tropopause height data. However, this result indicates that deep convective clouds have more potential to penetrate the stratosphere inside TCs than outside TCs, consistent with the results of Romps and Kuang (2009).

As mentioned in the introduction, knowledge of the vertical distribution of clouds is still lacking in TCs, especially in terms of individual cloud types. The 2B-CLDCLASS-lidar product from the TC overpass dataset provides an opportunity to quantify the frequency of occurrence of cumulonimbus, cirrus, and other cloud types with unprecedented detail. These results are shown in Fig. 3. Convective regimes broadly consistent with the known structure of TCs (see Frank 1977) can be identified. The eyewall region corresponds to the local maximum of cumulonimbus occurrence frequency inside the 100-km radius, extending to near-tropopause altitudes and associated with a local minimum in cirrus occurrence frequency. Inner rainbands are visible between 100 and 225 km with median cloud top heights above 15 km and an interquartile range extending to lower altitudes than for the eyewall region. The outer spiral rainband region between 225 and 500 km is characterized by median cloud top heights above 14.5 km and a large interquartile range. Outside 500 km, the median cloud top height varies significantly and the total cloud cover decreases, consistent with suppressed or sporadic convection.

In much of the TTL (14–18.5 km) and at all radii, cirrus and cumulonimbus account for over 80% of the total cloud cover (Fig. 3c). Qualitatively speaking (from Fig. 1), it is reasonable to expect longwave cooling of the tropopause in the eyewall region due to the frequent presence of optically thick convective clouds. At larger radius, the presence of high-altitude cirrus above a rapidly decreasing cumulonimbus cover can also be qualitatively expected to produce longwave warming near the tropopause. Both these effects are quantified in section 3d.

b. Tropopause layer cooling derived from COSMIC temperature retrievals

Next, we quantify the temperature tendency in the TTL corresponding to TLC. Figure 4a shows the temperature tendency as a function of radius and altitude. The temperature tendency is calculated as the slope of the linear regression between the median temperature and time, at each radius and altitude. This calculation implies that the tendencies in Fig. 4a include a contribution from changes in the mean thermal structure of the atmosphere along TC tracks. The contribution from the mean atmosphere includes processes that are not unique to TCs, shown in Fig. 4b in gray. The evolution of the mean tropopause is qualitatively similar to that within TCs. This is due to the average TC track in the western North Pacific following a path from near 13°N, 148°E toward colder and higher tropopauses near 20°N, 125°E during the 4 days leading to maximum intensity. A more detailed discussion is presented in the appendix. Qualitatively speaking, removing the contribution of the mean atmosphere from the total tendency does not change the general interpretation of the results; it reduces the magnitude of the tendencies in Fig. 4a, but still leads to a robust, large-scale signal of the same order of magnitude. For this reason, and for simplicity, the contribution of the mean atmosphere is not removed from Fig. 4a. We remind the reader that in this study, the order of magnitude of temperature tendencies derived from COSMIC and their overall spatial distribution are more important than fine details and variability. This constraint is primarily due to the nature of the COSMIC dataset and the length of its record.

The temperature tendencies in Fig. 4a are also subject to abrupt changes in the thermal structure of the TTL near the subtropical jet; the temperature difference between air masses with tropical and subtropical characteristics produces large tendencies that are not directly related to TCs. To minimize this effect, temperature retrievals are excluded from Fig. 4a when they exhibit subtropical characteristics. The method employed to this end is explained in the appendix.

The lower stratosphere exhibits a cooling rate of order $0.1–1\,K\,day^{-1}$ on horizontal scales of $\sim$1000 km, with a maximum amplitude found just above the median tropopause inside the 250-km radius. The upper troposphere exhibits a warming of slightly smaller amplitude with a maximum amplitude at small radii near 15-km altitude. The median tropopause height varies by $\sim$300 m (16.7–17 km) over the range of radii shown, and its interquartile range extends from 16.3 to 17.4 km. Its time dependency is of order $100\,m\,day^{-1}$, associated with cooling $\sim$0.5 K day^{-1} (Fig. 4b). The height of the tropopause within TCs is expectedly more variable than the height of the climatological
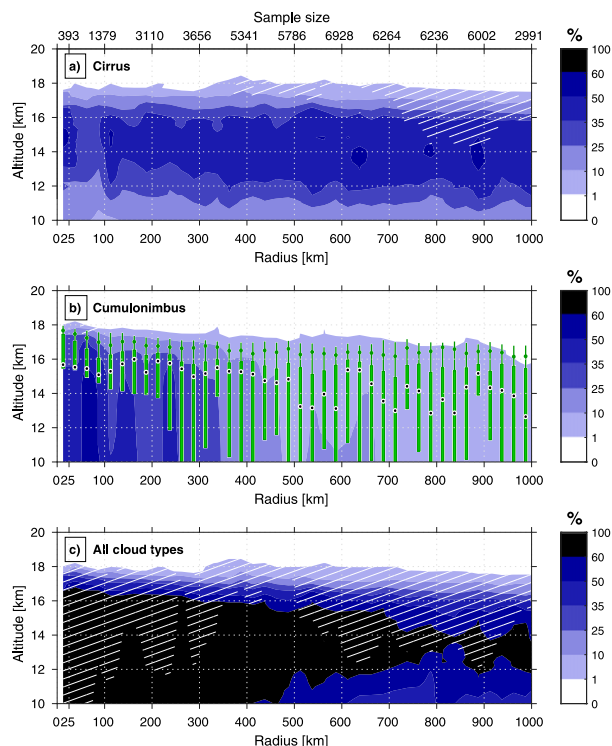
FIG. 3. Frequency of occurrence of (a) cirrus, (b) cumulonimbus, and (c) all cloud types, expressed at each radius and altitude as the percentage of all available 2B-CLDCLASS-lidar data that contain hydrometeors classified as either cloud type. The white hatching indicates where (a) cirrus, (b) cumulonimbus, and (c) cirrus and cumulonimbus together account for at least 80% of the total cloud fraction. Green boxplots show statistics of the cloud top height for cumulonimbus: the median (circled dots), the interquartile range (rectangles), and the 90th percentiles (small green circles on vertical lines that extend to the 99th percentile). The horizontal resolution is 25 km. Sample size is linearly interpolated to a regular grid for clarity.

tropopause (for which the interquartile range is 16.6–17.2 km). The tropopause is slightly lower than the climatological median (16.9 km) except at small radii.

The determination coefficient R^2 (hatching in Fig. 4a) gives a general idea of the robustness of the signal. Another way to quantify the robustness of the signal is to produce composites with random resampling of the dataset (bootstrapping). This alternative method (not shown for conciseness) provides nearly identical results. It should also be noted that using a linear regression to estimate temperature tendencies from COSMIC retrievals is not a choice as much as it is a constraint: the size of the COSMIC dataset limits the temporal resolution with which robust temperature composites can be produced, in turn narrowing the choice of method.

c. Radiative effect of the CB, MIX, and CI cloud scenarios

With total temperature tendency estimates in hand, we proceed to quantify the contribution of cloud radiative

effects from the three cloud scenarios that impact the tropopause (CB, MIX, and CI). Figure 5 shows the typical cloud-type profiles, cloudy-sky longwave heating rates, and clear-sky longwave heating rates corresponding to each cloud scenario. The MIX scenario is separated into MIX− and MIX+ depending on the average longwave heating rate between 16 and 18 km (see Fig. 5a). The expected qualitative longwave effects illustrated in Fig. 1 are verified: within the 16–18-km layer, the CB scenario produces cooling, the CI scenario produces warming, and the MIX scenario produces cooling (MIX−) when clouds below are mostly deep convective and warming (MIX+) when clouds below are stratocumuliform or stratiform in nature. The vast majority of MIX cases are composed of cirrus above 10 km (over 80% of them for MIX+). CB produces cooling of order 1–2 K day^{-1} near the tropopause and 2–10 K day^{-1} just below. CI produces warming up to ~2.5 K day^{-1} below the tropopause. MIX− can produce cooling up to ~1 K day^{-1} and MIX+ warming up to ~2.5 K day^{-1} just below the tropopause.

The CB and MIX− scenarios produce median radiative heating rates on the same order of magnitude as the total temperature tendencies seen at the tropopause and just below it (Fig. 4a). The 25th percentiles of heating rates for the CB scenario are 1–2 orders of magnitude larger than observed temperature tendencies. These heating rates occur ~1% of the time and are associated with larger ice water content and radar reflectivity (not shown). These heating rates also maximize near 16 km (i.e., below the largest tendencies associated with TLC). Neither the CB nor MIX− scenario produces radiative heating rates that are large enough to explain the temperature tendencies seen above the tropopause. Considering the shortwave contribution (not shown), which is equal to or greater than zero, the net radiative effect of these cloud scenarios seems unlikely to explain TLC. One potential exception is the occurrence of the CB scenario during nighttime (when shortwave heating is zero). The clear-sky radiative heating rates (Fig. 5c) change sign near 15 km and show a warming up to 0.5 K day^{-1} near the tropopause, consistent with previous results showing absorption of longwave radiation by elevated ozone concentrations in the lower stratosphere and a negligible contribution from water vapor (e.g., Gettelman et al. 2004). The rest of the troposphere displays the typical ~2 K day^{-1} clear-sky cooling rate.

As can be expected from the radial structure of cloud occurrence frequencies in Fig. 3, different cloud scenarios tend to occur at different radii within TCs: the median radius of occurrence for the CB, MIX−, MIX+, and CI scenarios is 328, 506, 608, and 637 km, respectively. This has bearing on the overall effect of clouds near the tropopause (see section 3d).
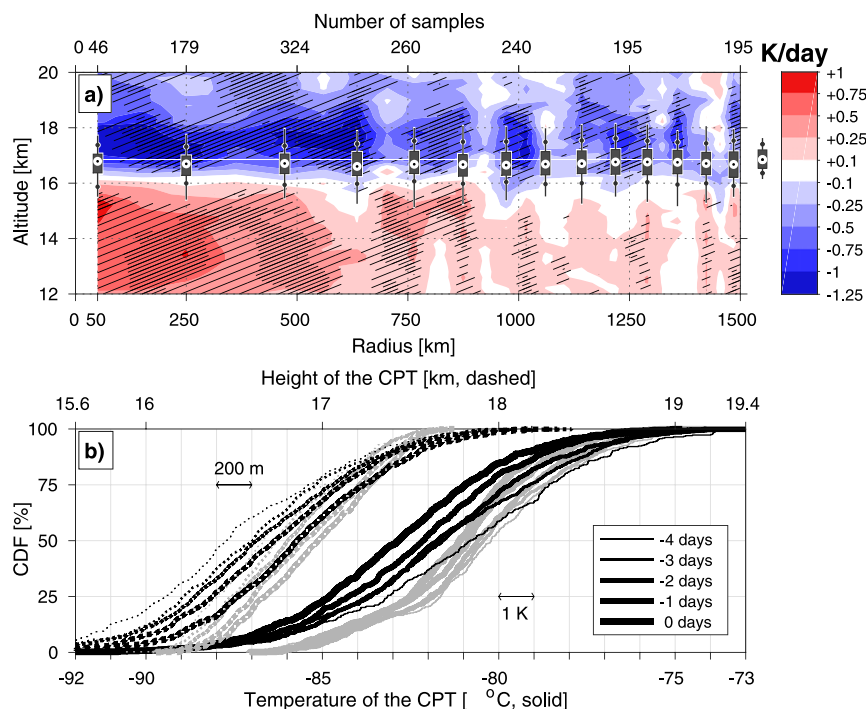
FIG. 4. (a) Temperature tendency (K day^{-1}), defined at each radius and altitude as the slope of the linear regression between the median temperature and time (relative to maximum intensity). Hatching indicates tendencies for which the coefficient of determination R^2 of the regression exceeds 0.6 in absolute value, and is doubled where R^2 exceeds 0.8. Boxplots show the median height of the tropopause (circled dots) with rectangles showing the interquartile range, whiskers extending from the 1st to the 99th percentiles, and small circles indicating the 10th and 90th percentiles. The white, thin horizontal line emphasizes the median height of the climatological tropopause between 0 and 1500 km (16.9 km), for which statistics are provided in the boxplot outside the main axis. The vertical resolution is 200 m. The horizontal resolution is a function of radius so as to homogenize the sample size between radial bins and is 100 km (30 km) at the 250-km (1500-km) radius. Sample size is linearly interpolated to a regular grid for clarity. (b) Cumulative distribution functions of the height (dashed) and temperature (solid) of the cold-point tropopause (CPT) between 0 and 1000 km, as a function of time relative to the time of maximum intensity (see legend). Black lines show data associated with active TCs, and gray lines show the monthly climatology interpolated onto the location of active TCs.

d. Gross radiative effect of clouds in the TTL

Last, we quantify the overall effect of clouds in the TTL (i.e., the weighted effects of the cloud scenarios analyzed earlier, plus the contribution from other cloud scenarios that we did not isolate due to their relatively low occurrence frequency or complex nature). Figure 6a shows the median all-sky longwave heating rates as a function of radius and altitude, and Fig. 6b shows the cloudy-sky contribution. Statistics of the tropopause height are overlaid, as well as total temperature tendency outlines to facilitate visual comparison with the results from Fig. 4. We first note that the results are broadly consistent with the radial distribution of the cloud scenarios in section 3c; the

strongest cooling occurs near the center of the storm where the CB and MIX− cases have most frequently been observed, and cooling of smaller amplitude occurs at larger radii where the MIX+ and CI cases are more frequent.

From Fig. 6b it is clear that clouds associated with TCs have the potential to produce radiative cooling in the TTL. Inside the main convective region of TCs (i.e., inside ∼300 km), longwave cloud radiative heating rates are dominated by the occurrence of cumulonimbus (including the CB scenario); warming within cloud occurs below 14 km and cloud top cooling is visible between 14 and 16 km exhibiting magnitudes of the same order as TLC. Outside the main convective region around the tropopause (and over ∼90% of the area
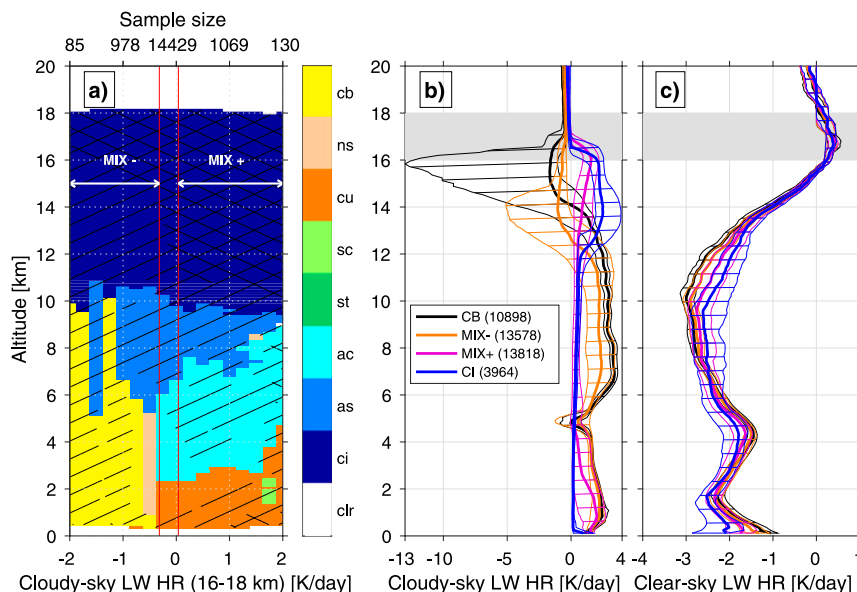
FIG. 5. (a) Most frequent cloud type encountered at each vertical level for the MIX scenario (clr: clear; ci: cirrus; as: altostratus; ac: altocumulus; st: stratus; sc: stratocumulus; cu: cumulus; ns: nimbostratus; cb: cumulonimbus). Black hatching (cross hatching) is used where the cloud type displayed is present at least 40% (80%) of the time. The abscissa is the cloudy-sky longwave heating rate averaged within the 16–18-km layer; the 25th ($-0.31 \, \mathrm{K \, day^{-1}}$) and 75th ($0.045 \, \mathrm{K \, day^{-1}}$) percentiles are indicated by two vertical red lines. These two values are used to separate the MIX cases that produce cooling (MIX−) or warming (MIX+) between 16 and 18 km. Cases that lie outside $\pm 2 \, \mathrm{K \, day^{-1}}$ are not included and represent less than 1% of the dataset. Sample size is linearly interpolated to a regular grid for clarity. (b) Median (thick lines) and interquartile range (hatched) cloudy-sky longwave heating rates and (c) clear-sky longwave heating rates for CB, CI, MIX−, and MIX+. The legend indicates the number of samples in each scenario. The 16–18-km layer is shaded in gray.

shown in the composites), longwave cloud radiative heating rates are about 5 times smaller than TLC. In this region, longwave warming occurs in much of the lower part of the TTL, in part corresponding to the occurrence of upper-tropospheric cirrus as shown in Fig. 3a. When adding to these features the clear-sky longwave contribution, the picture changes drastically (Fig. 6a). Cloud top cooling is only strong enough above the main convective region to counteract the tendency of clear-sky radiation to warm the upper part of the TTL.

Since the shortwave contribution is essentially zero during nighttime, Fig. 6a shows the net effect of radiation during nighttime. During daytime, one must account for the positive contribution of shortwave absorption by clouds and the atmosphere, which should be expected to be largest near the top of the main convective region. The shortwave heating rates from the radar–lidar products (not shown) suggest that the absorption of shortwave radiation can largely offset longwave cooling and lead to net warming near the top of the main convective region, while a net cooling remains in the upper troposphere outside the main convective region. Near

the tropopause, these heating rates suggest net daytime warming at all radii; that is, it is possible that the diurnal cycle of insolation acts in turn to increase and decrease TLC above the main convective region. This raises the question of the impact of the diurnal cycle on the feedbacks described in the introduction.

4. Discussion and conclusions

This study addresses mesoscale processes that act in synergy with synoptic-scale processes in TCs. Using the ability of A-Train satellites to detect both thick and thin clouds in the upper troposphere and lower stratosphere, we produce cloud type and cloud top height distributions within TCs (Figs. 2 and 3). We also use temperature retrievals from COSMIC to derive tropopause height statistics within TCs (Fig. 4). Last, we use radiative flux products from the A-Train satellites to provide quantitative evidence supporting the view that longwave cloud radiative effects only account for a fraction of the negative temperature tendencies observed on synoptic scales near the tropopause above TCs. Our
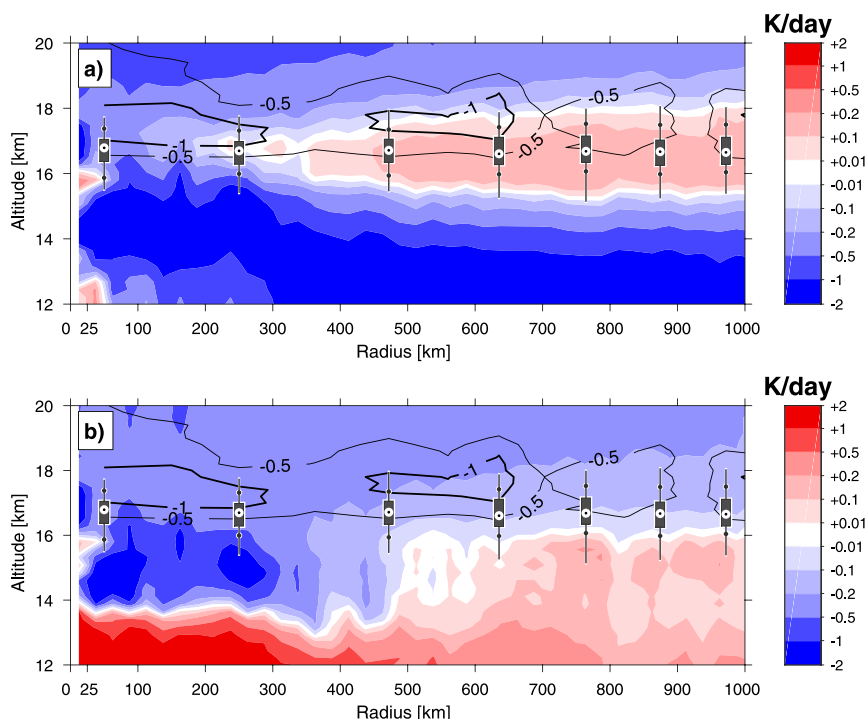
FIG. 6. (a) All-sky, median longwave heating rates and (b) cloudy-sky contribution. The boxplots (tropopause heights) and −0.5 and −1 K day^{-1} contours (temperature tendencies) are reproduced from Fig. 4a. The sample size is as in Fig. 3.

results (Fig. 5 and associated discussion) suggest that the all-sky net (longwave and shortwave) radiative effect is a warming of the tropopause and upper TTL over much of the area covered by TLC. Given that the potential for convection to reach and penetrate the stratosphere is greatest in the western North Pacific (Romps and Kuang 2009), we expect this general finding to hold for other oceanic basins (although this has not yet been verified). We also expect this finding to be valid for deep convection outside TCs, since deep convection does not reach near-tropopause altitudes outside TCs as often as it does inside TCs. While some cloud scenarios significantly affect the TTL below the tropopause, their effect above the tropopause is too small to explain the temperature tendencies there. We suggest that other mechanisms must play a predominant role in producing TLC, particularly outside the main convective region of TCs. Such mechanisms were introduced by previous literature (e.g., Johnson and Kriete 1982) but their relative contributions and spatial partitions remain uncertain.

On a fundamental level, TLC can be understood as a hydrostatic response to the presence of the warm core in the troposphere; given the constraint that horizontal pressure gradients must decrease with height and eventually vanish, cooling must occur somewhere in the column to compensate for horizontal pressure gradients associated with the warm core. However, the detailed mechanisms at play remain uncertain. Generally speaking, a source of heat generates a circulation that extends above the source and leads to net cooling where the vertical velocity is larger than the ratio of the heating rate to the static stability (Holloway and Neelin 2007). This leads to the formation of a cold anomaly just above the heat source, a phenomenon called the "convective cold top" by Holloway and Neelin (2007). In the upper troposphere and lower stratosphere where static stability becomes large and latent heat release is small, cooling can be expected even for small vertical velocities. In the context of a vortex in gradient wind and hydrostatic balance, the same phenomenon occurs (Eliassen 1951; Shapiro and Willoughby 1982) and the vertical expansion of the secondary circulation as a result of vortex strengthening can theoretically produce upward motion and divergence above the tropopause (Schubert and McNoldy 2010), thereby triggering a response not unlike TLC. This process is illustrated in Fig. 7 along with a schematic view of the relative positions of the tropopause, outflow layer, and typical cloud features relevant for our study. Beyond balanced vortex dynamics, recent literature (Cohen et al. 2017) raises the possibility that the conditions for gradient wind balance may
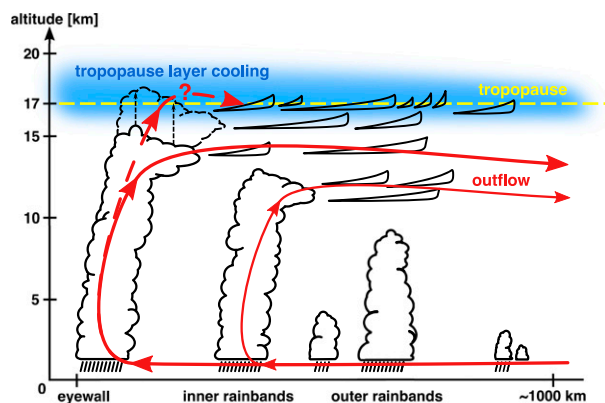
FIG. 7. Schematic summary of the TC structure and dynamics aspects relevant to this study; mainly the relative vertical position of the tropopause and tropopause layer cooling, cloud tops, and outflow layer. Horizontal axis not to scale; vertical axis is approximate. Some aspects of the circulation and cloud structure are omitted for clarity.

be violated in the upper troposphere above TCs, indicating that gradient imbalance and corresponding circulations should not be overlooked in the search to explain TLC.

Other processes may also cool the tropopause. Direct adiabatic cooling by cloud tops that overshoot their level of neutral buoyancy has often been invoked (Arakawa 1951; Koteswaram 1967; Sherwood et al. 2003; Kuang and Bretherton 2004; Robinson and Sherwood 2006). However, subsidence and compensating adiabatic warming can be expected on mesoscales as a response to overshooting, let alone the challenges inherent to the observation of short-lived, small-scale features such as overshooting tops. Fritsch and Brown (1982) have shown that overshooting tops modulate the response of the atmosphere near the tropopause above continental convective systems; however, it remains unclear whether this holds for marine convective systems in which vertical velocities are smaller and overshooting is less frequent [as mentioned by Sherwood et al. (2003)]. Results in Figs. 2b and 3b seem broadly consistent with the suggestion by Johnson and Kriete (1982) that overshooting clouds may radiatively cool the stratosphere by occasionally injecting ice into it—although we cannot directly quantify this effect.

Yet another phenomenon with potential to cool the tropopause is the propagation of convectively generated gravity waves from the main convective region. These waves—which do not require overshooting and are observed at great distances from their source (see Fritts and Alexander 2003, and references therein)—grow rapidly in magnitude in the lower stratosphere and trigger ascent and substantial temperature variability near the tropopause (Randel et al. 2003; Randel and Wu 2005). It remains uncertain how gravity waves interact to produce net cooling.

A few nuances are worth mentioning that should be kept in mind when interpreting our results. The potential impact of cloud radiative effects on the TC outflow layer (in the upper troposphere below the tropopause) is to be interpreted carefully. Our azimuthally averaged composites are only relevant to the symmetrical component of the TC structure, which can be rather small for the outflow where it is channeled in an asymmetric fashion by the large-scale environment (outside the 400-km radius; see Black and Anthes 1971). Further data and greater sampling frequency are needed in order to alleviate this limitation. Other limitations related to the *CloudSat* data products include uncertainties in the heating rates linked to the assumption of hydrometeor sphericity (Zhang et al. 2009) and inaccuracies in the estimates of meteorological variables and active species (ozone, water vapor). Resolving these limitations will require, broadly, better instrumentation and more accurate global analyses. Last, sun-asynchronous data will be needed in order to understand the effect of the diurnal cycle on convection and on the TTL.

APPENDIX

Calculation of Temperature Tendencies

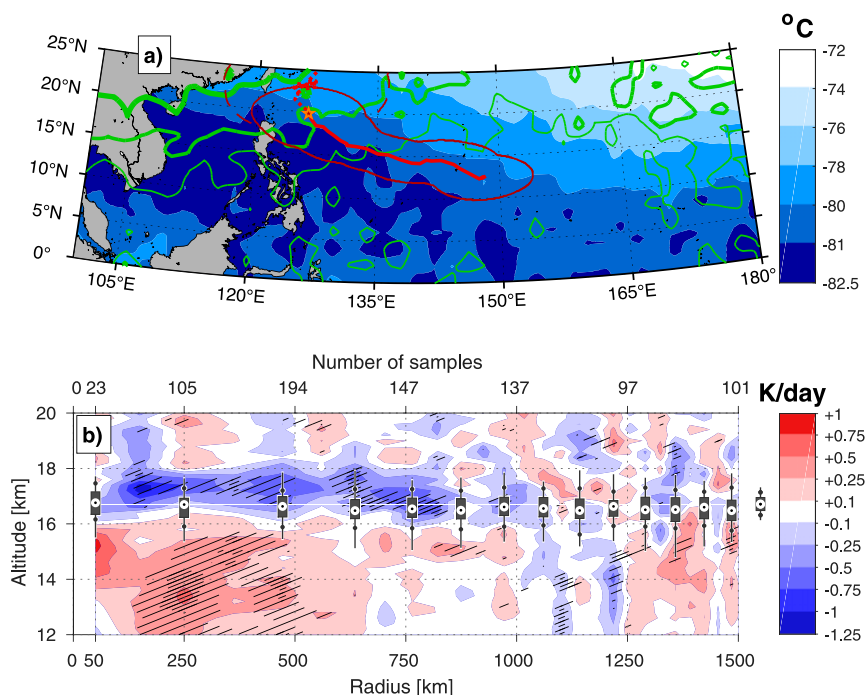Details of the method employed to calculate the temperature tendencies shown in Fig. 4a are discussed here.

FIG. A1. (a) Average temperature of the cold-point tropopause (shaded; note the spacing of the color scheme) for August–October, weighted by the number of TCs developing each month. The average height of the cold-point tropopause is shown as green isolines (16.6, 16.8, and 17 km, from thin to thick). The average TC track is in red, with the area delimited by a thin red line showing ±1 standard deviation from the average track. The star indicates the location of the average lifetime maximum intensity. Best track data collected after maximum intensity are dashed. (b) As in Fig. 4a, but for August–October with the tendency associated with the monthly climatology removed.

The contribution of the mean atmosphere to the temperature tendencies in Fig. 4a arises from the latitudinal and longitudinal dependency of the mean thermal structure of the atmosphere. Figure A1a shows this structure at the level of the cold-point tropopause for August–October (the 3-month period with the most TC activity). Figure A1a reveals that the tropopause rises and cools along the average TC track during intensification, leading to negative tendencies near the tropopause on average. In parallel, the average temperature of the upper troposphere increases along the average TC track (not shown), leading to positive tendencies in the troposphere. Figure A1b illustrates how removing the background tendency from the tendency in Fig. 4a yields decreased amplitudes, but the qualitative nature of the signal and its order of magnitude are largely preserved: robust cooling still exists near the tropopause and in the lower stratosphere on spatial scales that exceed those of the cloud top cooling shown in Fig. 6b. Tendencies in Fig. A1b are least robust at large radii where the composite includes influences from the atmosphere on the equatorward and poleward sides of

TC tracks. It should be mentioned that the background tendency in Fig. A1b is evaluated along each TC track rather than along the average TC track shown in Fig. A1a; the average track is only shown for qualitative purposes.

As noted in section 3b, the temperature tendencies in Fig. A1a exclude temperature retrievals that exhibit subtropical characteristics. A simple method is chosen to distinguish temperature retrievals with tropical and subtropical characteristics: a temperature retrieval is considered tropical when the height of its lapse-rate tropopause (LRT; definition from WMO 1957) is located within 400 m of the height of its cold-point tropopause (CPT). The choice of criterion is motivated by results in Pan et al. (2018) and by the scatterplots in Fig. A2. Tropical air masses typically exhibit a sharp change in sign of the lapse rate around the tropopause, yielding similar heights for the CPT and the LRT. Air masses subject to subtropical influence typically exhibit lapse-rate inversions in shallow layers below the CPT, yielding a lower LRT. Around 20% of the COSMIC retrievals sampled in this study exhibit subtropical characteristics.
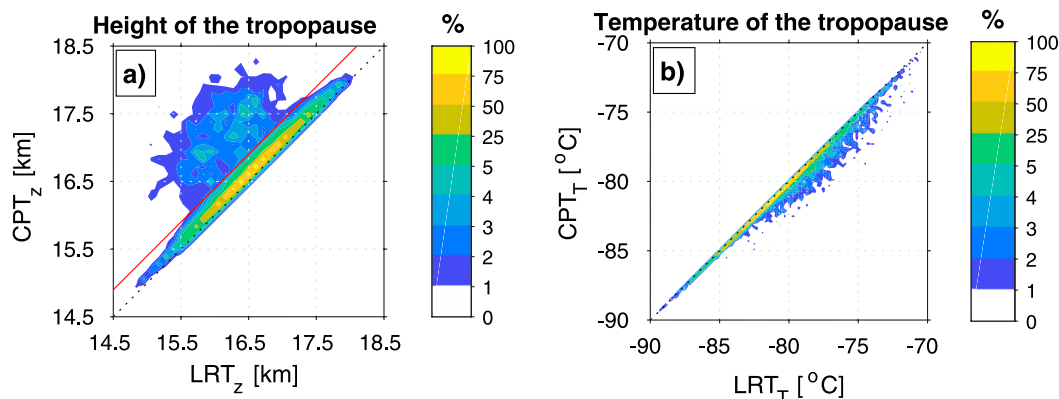
FIG. A2. Relationship between (a) the height and (b) the temperature of the cold-point tropopause (CPT) and of the lapse-rate tropopause (LRT), shown as frequency of occurrence for August–October. The red line in (a) is 400 m above of the 1:1 line (dotted) and is used to separate air masses with tropical and subtropical characteristics. Note the spacing of the color scheme.

REFERENCES

Ackerman, T. P., K.-N. Liou, F. P. Valero, and L. Pfister, 1988: Heating rates in tropical anvils. *J. Atmos. Sci.*, **45**, 1606–1623, https://doi.org/10.1175/1520-0469(1988)045<1606:HRITA>2.0.CO;2.

Alcala, C., and A. Dessler, 2002: Observations of deep convection in the tropics using the Tropical Rainfall Measuring Mission (TRMM) precipitation radar. *J. Geophys. Res.*, **107**, 4792, https://doi.org/10.1029/2002JD002457.

Angell, J. K., and J. Korshover, 1964: Quasi-biennial variations in temperature, total ozone, and tropopause height. *J. Atmos. Sci.*, **21**, 479–492, https://doi.org/10.1175/1520-0469(1964)021<0479:QBVITT>2.0.CO;2.

Anthes, R. A., and Coauthors, 2008: The COSMIC/FORMOSAT-3 mission: Early results. *Bull. Amer. Meteor. Soc.*, **89**, 313–334, https://doi.org/10.1175/BAMS-89-3-313.

Arakawa, H., 1951: Analysis of the tropopause and the stratospheric field of temperature of a mature typhoon. *Pap. Meteor. Geophys.*, **2** (1), 1–5, https://doi.org/10.2467/mripapers1950.2.1_1.

Austin, R. T., A. J. Heymsfield, and G. L. Stephens, 2009: Retrieval of ice cloud microphysical parameters using the CloudSat millimeter-wave radar and temperature. *J. Geophys. Res.*, **114**, D00A23, https://doi.org/10.1029/2008JD010049.

Biondi, R., S.-P. Ho, W. Randel, S. Syndergaard, and T. Neubert, 2013: Tropical cyclone cloud-top height and vertical temperature structure detection using GPS radio occultation measurements. *J. Geophys. Res.*, **118**, 5247–5259, https://doi.org/10.1002/JGRD.50448.

Birner, T., and E. J. Charlesworth, 2017: On the relative importance of radiative and dynamical heating for tropical tropopause temperatures. *J. Geophys. Res. Atmos.*, **122**, 6782–6797, https://doi.org/10.1002/2016JD026445.

Black, P. G., and R. A. Anthes, 1971: On the asymmetric structure of the tropical cyclone outflow layer. *J. Atmos. Sci.*, **28**, 1348–1366, https://doi.org/10.1175/1520-0469(1971)028<1348:OTASOT>2.0.CO;2.

Cairo, F., and Coauthors, 2008: Morphology of the tropopause layer and lower stratosphere above a tropical cyclone: A case study on Cyclone Davina (1999). *Atmos. Chem. Phys.*, **8**, 3411–3426, https://doi.org/10.5194/acp-8-3411-2008.

Chen, H., and D.-L. Zhang, 2013: On the rapid intensification of Hurricane Wilma (2005). Part II: Convective bursts and the upper-level warm core. *J. Atmos. Sci.*, **70**, 146–162, https://doi.org/10.1175/JAS-D-12-062.1.

Cohen, Y., N. Harnik, E. Heifetz, D. S. Nolan, D. Tao, and F. Zhang, 2017: On the violation of gradient wind balance at the top of tropical cyclones. *Geophys. Res. Lett.*, **44**, 8017–8026, https://doi.org/10.1002/2017GL074552.

Corti, T., B. Luo, T. Peter, H. Vömel, and Q. Fu, 2005: Mean radiative energy balance and vertical mass fluxes in the equatorial upper troposphere and lower stratosphere. *Geophys. Res. Lett.*, **32**, L06802, https://doi.org/10.1029/2004GL021889.

Danielsen, E. F., 1993: In situ evidence of rapid, vertical, irreversible transport of lower tropospheric air into the lower tropical stratosphere by convective cloud turrets and by larger-scale upwelling in tropical cyclones. *J. Geophys. Res.*, **98**, 8665–8681, https://doi.org/10.1029/92JD02954.

Davis, N., and T. Birner, 2016: Climate model biases in the width of the tropical belt. *J. Climate*, **29**, 1935–1954, https://doi.org/10.1175/JCLI-D-15-0336.1.

Doyle, J. D., and Coauthors, 2017: A view of tropical cyclones from above: The Tropical Cyclone Intensity Experiment. *Bull. Amer. Meteor. Soc.*, **98**, 2113–2134, https://doi.org/10.1175/BAMS-D-16-0055.1.

Eliassen, A., 1951: Slow thermally or frictionally controlled meridional circulation in a circular vortex. *Astrophys. Norv.*, **5**, 19–60.

Flatau, M., and D. E. Stevens, 1993: The role of outflow-layer instabilities in tropical cyclone motion. *J. Atmos. Sci.*, **50**, 1721–1733, https://doi.org/10.1175/1520-0469(1993)050<1721:TROOLI>2.0.CO;2.

Frank, W. M., 1977: The structure and energetics of the tropical cyclone I. Storm structure. *Mon. Wea. Rev.*, **105**, 1119–1135, https://doi.org/10.1175/1520-0493(1977)105<1119:TSAEOT>2.0.CO;2.

Fritsch, J., and J. Brown, 1982: On the generation of convectively driven mesohighs aloft. *Mon. Wea. Rev.*, **110**, 1554–1563, https://doi.org/10.1175/1520-0493(1982)110<1554:OTGOCD>2.0.CO;2.

Fritts, D. C., and M. J. Alexander, 2003: Gravity wave dynamics and effects in the middle atmosphere. *Rev. Geophys.*, **41**, 1003, https://doi.org/10.1029/2001RG000106.

Fu, Q., and K. Liou, 1992: On the correlated k-distribution method for radiative transfer in nonhomogeneous atmospheres. *J. Atmos. Sci.*, **49**, 2139–2156, https://doi.org/10.1175/1520-0469(1992)049<2139:OTCDMF>2.0.CO;2.

Fueglistaler, S., A. Dessler, T. Dunkerton, I. Folkins, Q. Fu, and P. W. Mote, 2009: Tropical tropopause layer. *Rev. Geophys.*, **47**, RG1004, https://doi.org/10.1029/2008RG000267.

Gettelman, A., M. Salby, and F. Sassi, 2002: Distribution and influence of convection in the tropical tropopause region. *J. Geophys. Res.*, **107**, 4080, https://doi.org/10.1029/2001JD001048.

——, P. M. F. Forster, M. Fujiwara, Q. Fu, H. Vömel, L. K. Gohar, C. Johanson, and M. Ammerman, 2004: Radiation balance of the tropical tropopause layer. *J. Geophys. Res.*, **109**, D07103, https://doi.org/10.1029/2003JD004190.

Hahn, C. J., and S. G. Warren, 1999: Extended edited synoptic cloud reports from ships and land stations over the globe, 1952–1996. Tech. Rep. NDP026C, Carbon Dioxide Information Analysis Center, Oak Ridge National Laboratory, 71 pp.

Hartmann, D. L., J. R. Holton, and Q. Fu, 2001: The heat balance of the tropical tropopause, cirrus, and stratospheric dehydration. *Geophys. Res. Lett.*, **28**, 1969–1972, https://doi.org/10.1029/2000GL012833.

Hawkins, J. D., F. J. Turk, T. F. Lee, and K. Richardson, 2008: Observations of tropical cyclones with the SSMIS. *IEEE Trans. Geosci. Remote Sens.*, **46**, 901–912, https://doi.org/10.1109/TGRS.2008.915753.

Haynes, J. M., T. S. L'Ecuyer, G. L. Stephens, S. D. Miller, C. Mitrescu, N. B. Wood, and S. Tanelli, 2009: Rainfall retrieval over the ocean with spaceborne W-band radar. *J. Geophys. Res.*, **114**, D00A22, https://doi.org/10.1029/2008JD009973.

Henderson, D. S., T. L'Ecuyer, G. Stephens, P. Partain, and M. Sekiguchi, 2013: A multisensor perspective on the radiative impacts of clouds and aerosols. *J. Appl. Meteor. Climatol.*, **52**, 853–871, https://doi.org/10.1175/JAMC-D-12-025.1.

Holland, G. J., and R. T. Merrill, 1984: On the dynamics of tropical cyclone structural changes. *Quart. J. Roy. Meteor. Soc.*, **110**, 723–745, https://doi.org/10.1002/qj.49711046510.

Holloway, C. E., and J. D. Neelin, 2007: The convective cold top and quasi equilibrium. *J. Atmos. Sci.*, **64**, 1467–1487, https://doi.org/10.1175/JAS3907.1.

Jensen, E. J., O. B. Toon, H. B. Selkirk, J. D. Spinhirne, and M. R. Schoeberl, 1996: On the formation and persistence of subvisible cirrus clouds near the tropical tropopause. *J. Geophys. Res.*, **101**, 21 361–21 375, https://doi.org/10.1029/95JD03575.

——, A. Ackerman, and J. Smith, 2007: Can overshooting convection dehydrate the tropical tropopause layer? *J. Geophys. Res.*, **112**, D11209, https://doi.org/10.1029/2006JD007943.

Johnson, R. H., and D. C. Kriete, 1982: Thermodynamic and circulation characteristics of winter monsoon tropical mesoscale convection. *Mon. Wea. Rev.*, **110**, 1898–1911, https://doi.org/10.1175/1520-0493(1982)110<1898:TACCOW>2.0.CO;2.

Jordan, C., 1960: Abnormally cold tropopause temperatures in the equatorial Pacific. *Mon. Wea. Rev.*, **88**, 151–154, https://doi.org/10.1175/1520-0493(1960)088<0151:ACTTIT>2.0.CO;2.

Kim, J., W. J. Randel, and T. Birner, 2018: Convectively driven tropopause-level cooling and its influences on stratospheric moisture. *J. Geophys. Res. Atmos.*, **123**, 590–606, https://doi.org/10.1002/2017JD027080.

Knaff, J. A., D. P. Brown, J. Courtney, G. M. Gallina, and J. L. Beven, 2010: An evaluation of Dvorak technique–based tropical cyclone intensity estimates. *Wea. Forecasting*, **25**, 1362–1379, https://doi.org/10.1175/2010WAF2222375.1.

——, S. P. Longmore, R. T. DeMaria, and D. A. Molenar, 2015: Improved tropical-cyclone flight-level wind estimates using routine infrared satellite reconnaissance. *J. Appl. Meteor. Climatol.*, **54**, 463–478, https://doi.org/10.1175/JAMC-D-14-0112.1.

——, C. J. Slocum, and K. D. Musgrave, 2019: Quantification and exploration of diurnal oscillations in tropical cyclones. *Mon. Wea. Rev.*, **147**, 2105–2121, https://doi.org/10.1175/MWR-D-18-0379.1.

Koteswaram, P., 1967: On the structure of hurricanes in the upper troposphere and lower stratosphere. *Mon. Wea. Rev.*, **95**, 541–564, https://doi.org/10.1175/1520-0493(1967)095<0541:OTSOHI>2.3.CO;2.

Kuang, Z., and C. S. Bretherton, 2004: Convective influence on the heat balance of the tropical tropopause layer: A cloud-resolving model study. *J. Atmos. Sci.*, **61**, 2919–2927, https://doi.org/10.1175/JAS-3306.1.

Kuo, Y.-H., T.-K. Wee, S. Sokolovskiy, C. Rocken, W. Schreiner, D. Hunt, and R. Anthes, 2004: Inversion and error estimation of GPS radio occultation data. *J. Meteor. Soc. Japan*, **82**, 507–531, https://doi.org/10.2151/JMSJ.2004.507.

Kursinski, E., and Coauthors, 1996: Initial results of radio occultation observations of Earth's atmosphere using the Global Positioning System. *Science*, **271**, 1107–1110, https://doi.org/10.1126/science.271.5252.1107.

——, G. Hajj, J. Schofield, R. Linfield, and K. R. Hardy, 1997: Observing Earth's atmosphere with radio occultation measurements using the Global Positioning System. *J. Geophys. Res.*, **102**, 23 429–23 465, https://doi.org/10.1029/97JD01569.

L'Ecuyer, T. S., N. B. Wood, T. Haladay, G. L. Stephens, and P. W. Stackhouse Jr., 2008: Impact of clouds on atmospheric heating based on the R04 CloudSat fluxes and heating rates data set. *J. Geophys. Res.*, **113**, D00A15, https://doi.org/10.1029/2008JD009951.

Liu, C., and E. J. Zipser, 2008: Diurnal cycles of precipitation, clouds, and lightning in the tropics from 9 years of TRMM observations. *Geophys. Res. Lett.*, **35**, L04819, https://doi.org/10.1029/2007GL032437.

Mace, G. G., Q. Zhang, M. Vaughan, R. Marchand, G. Stephens, C. Trepte, and D. Winker, 2009: A description of hydrometeor layer occurrence statistics derived from the first year of merged CloudSat and CALIPSO data. *J. Geophys. Res.*, **114**, D00A26, https://doi.org/10.1029/2007JD009755.

Neumann, C. J., 1993: Global overview. Global Guide to Tropical Cyclone Forecasting, WMO/TD-560, World Meteorological Organization, 1.1–1.42.

Ohno, T., and M. Satoh, 2015: On the warm core of a tropical cyclone formed near the tropopause. *J. Atmos. Sci.*, **72**, 551–571, https://doi.org/10.1175/JAS-D-14-0078.1.

Pan, L. L., S. B. Honomichl, T. V. Bui, T. Thornberry, A. Rollins, E. Hintsa, and E. J. Jensen, 2018: Lapse rate or cold point: The tropical tropopause identified by in situ trace gas measurements. *Geophys. Res. Lett.*, **45**, 10 756–10 763, https://doi.org/10.1029/2018GL079573.

Paulik, L. C., and T. Birner, 2012: Quantifying the deep convective temperature signal within the tropical tropopause layer (TTL). *Atmos. Chem. Phys.*, **12**, 12 183–12 195, https://doi.org/10.5194/acp-12-12183-2012.

Randel, W. J., and F. Wu, 2005: Kelvin wave variability near the equatorial tropopause observed in GPS radio occultation measurements. *J. Geophys. Res.*, **110**, D03102, https://doi.org/10.1029/2004JD005006.

——, ——, and W. Rivera Ríos, 2003: Thermal variability of the tropical tropopause region derived from GPS/MET observations. *J. Geophys. Res.*, **108**, 4024, https://doi.org/10.1029/2002JD002595.

Ray, E. A., and K. H. Rosenlof, 2007: Hydration of the upper troposphere by tropical cyclones. *J. Geophys. Res.*, **112**, D12311, https://doi.org/10.1029/2006JD008009.

Reid, G. C., and K. S. Gage, 1985: Interannual variations in the height of the tropical tropopause. *J. Geophys. Res.*, **90**, 5629–5635, https://doi.org/10.1029/JD090iD03p05629.

Reynolds, R. W., and T. M. Smith, 1995: A high-resolution global sea surface temperature climatology. *J. Climate*, **8**, 1571–1583, https://doi.org/10.1175/1520-0442(1995)008<1571:AHRGSS>2.0.CO;2.

Rivoire, L., T. Birner, and J. A. Knaff, 2016: Evolution of the upper-level thermal structure in tropical cyclones. *Geophys. Res. Lett.*, **43**, 10 530–10 537, https://doi.org/10.1002/2016GL070622.

Robinson, F., and S. Sherwood, 2006: Modeling the impact of convective entrainment on the tropical tropopause. *J. Atmos. Sci.*, **63**, 1013–1027, https://doi.org/10.1175/JAS3673.1.

Romps, D. M., and Z. Kuang, 2009: Overshooting convection in tropical cyclones. *Geophys. Res. Lett.*, **36**, L09804, https://doi.org/10.1029/2009GL037396.

Rossow, W. B., and R. A. Schiffer, 1999: Advances in understanding clouds from ISCCP. *Bull. Amer. Meteor. Soc.*, **80**, 2261–2287, https://doi.org/10.1175/1520-0477(1999)080<2261:AIUCFI>2.0.CO;2.

Sampson, C. R., and A. J. Schrader, 2000: The automated tropical cyclone forecasting system (version 3.2). *Bull. Amer. Meteor. Soc.*, **81**, 1231–1240, https://doi.org/10.1175/1520-0477(2000)081<1231:TATCFS>2.3.CO;2.

Sassen, K., and Z. Wang, 2008: Classifying clouds around the globe with the CloudSat radar: 1 year of results. *Geophys. Res. Lett.*, **35**, L04805, https://doi.org/10.1029/2007GL032591.

——, and ——, 2012: The clouds of the middle troposphere: Composition, radiative impact, and global distribution. *Surv. Geophys.*, **33**, 677–691, https://doi.org/10.1007/s10712-011-9163-x.

——, ——, and D. Liu, 2008: Global distribution of cirrus clouds from CloudSat/Cloud-Aerosol Lidar and Infrared Pathfinder Satellite Observations (CALIPSO) measurements. *J. Geophys. Res.*, **113**, D00A12, https://doi.org/10.1029/2008JD009972.

——, ——, and ——, 2009: Cirrus clouds and deep convection in the tropics: Insights from CALIPSO and CloudSat. *J. Geophys. Res.*, **114**, D00H06, https://doi.org/10.1029/2009JD011916.

Schubert, W. H., and B. D. McNoldy, 2010: Application of the concepts of Rossby length and Rossby depth to tropical cyclone dynamics. *J. Adv. Model. Earth Syst.*, **2**, 7, https://doi.org/10.3894/JAMES.2010.2.7.

Seidel, D. J., R. J. Ross, J. K. Angell, and G. C. Reid, 2001: Climatological characteristics of the tropical tropopause as revealed by radiosondes. *J. Geophys. Res.*, **106**, 7857–7878, https://doi.org/10.1029/2000JD900837.

Shapiro, L. J., and H. E. Willoughby, 1982: The response of balanced hurricanes to local sources of heat and momentum. *J. Atmos. Sci.*, **39**, 378–394, https://doi.org/10.1175/1520-0469(1982)039<0378:TROBHT>2.0.CO;2.

Sherwood, S. C., T. Horinouchi, and H. A. Zeleznik, 2003: Convective impact on temperatures observed near the tropical tropopause. *J. Atmos. Sci.*, **60**, 1847–1856, https://doi.org/10.1175/1520-0469(2003)060<1847:CIOTON>2.0.CO;2.

Stephens, G. L., P. M. Gabriel, and P. T. Partain, 2001: Parameterization of atmospheric radiative transfer. Part I: Validity of simple models. *J. Atmos. Sci.*, **58**, 3391–3409, https://doi.org/10.1175/1520-0469(2001)058<3391:POARTP>2.0.CO;2.

——, and Coauthors, 2002: The CloudSat mission and the A-Train: A new dimension of space-based observations of clouds and precipitation. *Bull. Amer. Meteor. Soc.*, **83**, 1771–1790, https://doi.org/10.1175/BAMS-83-12-1771.

Thuburn, J., and G. C. Craig, 2002: On the temperature structure of the tropical substratosphere. *J. Geophys. Res.*, **107**, 4017, https://doi.org/10.1029/2001JD000448.

Torn, R. D., and C. Snyder, 2012: Uncertainty of tropical cyclone best-track information. *Wea. Forecasting*, **27**, 715–729, https://doi.org/10.1175/WAF-D-11-00085.1.

Tourville, N., G. Stephens, M. DeMaria, and D. Vane, 2015: Remote sensing of tropical cyclones: Observations from *CloudSat* and A-Train profilers. *Bull. Amer. Meteor. Soc.*, **96**, 609–622, https://doi.org/10.1175/BAMS-D-13-00282.1.

Townshend, J. R., 1992: Improved global data for land applications: A proposal for a new high resolution data set. IGBP Global Change Rep. 20, 85 pp., http://www.igbp.net/download/18.950c2fa1495db7081e1942/1430900178610/IGBP_report_20-Global_Data_land.pdf.

Trepte, Q. Z., P. Minnis, C. R. Trepte, S. Sun-Mack, and R. Brown, 2010: Improved cloud detection in CERES Edition 3 algorithm and comparison with the CALIPSO Vertical Feature Mask. *Proc. 13th Conf. on Atmospheric Radiation and Cloud Physics*, Portland, OR, Amer. Meteor. Soc., JP1.32, https://ams.confex.com/ams/13CldPhy13AtRad/webprogram/Paper171785.html.

WMO, 1957: Meteorology—A three-dimensional science: Second session of the Commission for Aerology. *WMO Bull.*, **4**, 134–138.

Yang, Q., Q. Fu, and Y. Hu, 2010: Radiative impacts of clouds in the tropical tropopause layer. *J. Geophys. Res.*, **115**, D00H12, https://doi.org/10.1029/2009JD012393.

Zhang, D.-L., and H. Chen, 2012: Importance of the upper-level warm core in the rapid intensification of a tropical cyclone. *Geophys. Res. Lett.*, **39**, L02806, https://doi.org/10.1029/2011GL050578.

Zhang, Z., P. Yang, G. Kattawar, J. Riedi, L. Labonnote, B. Baum, S. Platnick, and H.-L. Huang, 2009: Influence of ice particle model on satellite ice cloud retrieval: Lessons learned from MODIS and POLDER cloud product comparison. *Atmos. Chem. Phys.*, **9**, 7115–7129, https://doi.org/10.5194/acp-9-7115-2009.